Collapse of a region of the magnetic phase diagram of elemental terbium under a strain-induced Lifshitz transition

A. Vl. Andrianov,[1] E. Mendive-Tapia,[2,*] A. I. Beskrovnyi,[3] and J. B. Staunton[4]
[1]*Department of Physics, Moscow State University, Moscow 119991, Russia*
[2]*Department of Computational Materials Design, Max-Planck-Institut für Eisenforschung, 40237 Düsseldorf, Germany*
[3]*Laboratory of Neutron Physics, Joint Institute for Nuclear Research, Dubna, Moscow District 141980, Russia*
[4]*Department of Physics, University of Warwick, Coventry CV4 7AL, United Kingdom*

(Received 2 November 2020; accepted 11 November 2021; published 24 November 2021)

AC susceptibility and neutron scattering measurements are used to study the magnetic field-temperature magnetic phase diagram of a Tb single crystal under uniaxial tension along its hexagonal c axis. An external magnetic field is applied in the basal plane. We focus on the region in the phase diagram that corresponds to the helical antiferromagnetic phase and find that this region collapses when the uniaxial tension is increased beyond a critical value as low as 600 bar. There are strong reasons to associate this collapse with an underlying Lifshitz transition in the Fermi surface of Tb's valence electrons. We use a finite-temperature *ab initio* theory to analyze our measurements, obtaining a pressure-temperature magnetic phase diagram in very good agreement with experiment. Our calculations indicate that short- and long-range magnetic order has a crucial effect on the Fermi surface nesting and consequent magnetism of Tb.

DOI: 10.1103/PhysRevB.104.174435

I. INTRODUCTION

The helical long-periodic antiferromagnetic (HAFM) structure, characteristic of several elemental rare-earth metals with hexagonal close-packed (hcp) crystalline structure and comprising a spiral staircase of the magnetic moments [1], remains perhaps one of the most elegant objects in solid state magnetism. The discovery of this structure in hcp elemental Ho, Dy and Tb was one of the first triumphs of the neutron scattering technique [2–4]. Immediately afterwards, a successful attempt to suppress the HAFM structure by the application of a magnetic field within the basal plane [5] led to the emergence of complex temperature-magnetic field phase diagrams. These uncovered a plethora of complex physics issues for the investigation of critical points and magnetic phase transitions in the rare earth elements. Today, despite continuous and extensive experimental and theoretical studies, many questions of fundamental interest still remain concerning the features of these diagrams.

The critical magnetic field values H^* required to suppress the HAFM phase turn out to be of the order of 10 000–20 000 Oe for Dy and Ho [5,6], which correspond to energies much lower than the exchange energy. Straightforward phenomenological analysis [7], as well as finite-temperature *ab initio* calculations carried out by us [8], agree that this suppression by magnetic field application takes two stages. A first transition occurs at H^* when the HAFM state collapses into an intermediate "near ferromagnetic" fan state, also long-periodic, where magnetic moments oscillate close to the magnetic field direction. The second one happens at H_{sat} when these oscillations vanish and a single-domain collinear ferromagnetic (FM) state is formed [1]. These transitions have been clearly observed in Dy, Ho, and their alloys with Y by various techniques, including magnetic measurements [9,10], neutron diffraction [5,11,12], magnetoresistance [13], acoustic studies [14–16], and x-ray diffraction [17–19].

Terbium appears to be a difficult object for such a study, as its HAFM state is delicate when compared to that in Dy and Ho and the associated anomalies are weak. The range of temperatures where the HAFM state occurs in Tb is remarkably narrow, less than 5% of the magnetic ordering temperature (hereafter referred to T_{ord} for both T_C or T_N). Tb is therefore poised right on the edge of being able to support helical magnetic order making its study interesting in its own right. Various studies report the magnitude of H^* to be around 100–500 Oe depending on the temperature and experimental technique used [20–24].

The relation between the stabilizing magnetic phase and the topology of the Fermi surface (FS) is an essential factor in the understanding of the magnetism of the hcp rare-earth metals. Namely, it is well established that the existence of the HAFM phase in these metals is directly governed by the shape of the FS through the "magnetic nesting" phenomenon, proposed for Cr by Lomer [25] and extended to rare-earth metals by Dzyaloshinski [26], see review [1]. As a consequence, the HAFM phase corresponds to the one plausible "yttriumlike" geometry of the FS, while the simple collinear ferromagnetic order is associated with the alternative "gadoliniumlike" geometry, see Refs. [8,27–34] for details.

These HAFM and ferromagnetic states are, therefore, separated by a Lifshitz transition in the conductive subsystem—i.e., the qualitative change in the shape [35] of the FS of

*Present address: Peter Grünberg Institut and Institute for Advanced Simulation, Forschungszentrum Jülich and JARA, 52425 Jülich, Germany.

the valence electrons. Consequently, this Lifshitz transition induced by external action—for example, by application of pressure—should change the type of magnetic order that stabilizes. The easiest way to induce this Lifshitz transition in the hcp rare-earth metal is to apply uniaxial strain along the hexagonal axis c, while isotropic hydrostatic pressure has a much smaller effect on the FS shape, see Ref. [32].

In Ref. [36], we demonstrated the total suppression of the HAFM ordering in favor of the simple ferromagnetic one under a critical uniaxial tension as low as 700 bar, which we associated with a Lifshitz transition in the FS of Tb. In parallel our progress with an *ab initio* electronic structure theory study of the heavy rare earth elements [8] has enabled us to determine the main features of the magnetic phase diagrams of the heavy lanthanide elements and to link a major component of the experimental features to the common valence electronic structure ($5d^1$ $6s^2$) that these elements share. The effect of stress, however, to date has not been explicitly calculated and presented. In this work, we report an experimental study for the magnetic phase diagram of Tb under uniaxial tension and the suppression of the HAFM phase via a Lifshitz transition. We show how the temperature-magnetic field phase diagram, critical magnetic field, and helical wave vector change with application of this pressure. We also compare our experimental results with our finite-temperature *ab initio* theory applied to Tb.

II. EXPERIMENTAL APPROACH

A. Experimental setup and neutron scattering study

As in Ref. [36], we measured the ac magnetic susceptibility χ_{ac}, by mutual inductance of two probe coils surrounding the sample—a reliable noncontact technique that directly reflects the magnetic state of the sample. In this study. we compared χ_{ac} dependencies for terbium that orders magnetically into the HAFM phase (at tensions below p^*) with those for the very same terbium sample that orders ferromagnetically (at tensions above p^*). This approach allows to highlight the apparently weak anomaly associated with the transition at H^*, which is the magnetic field necessary to suppress the HAFM phase at a given temperature.

The same single-crystalline sample and the same uniaxial tension cell as in Ref. [36] were employed in the present study, with now the addition of the permanent magnetic field; see detailed description and sample characterization in this reference. Both the ac and the permanent magnetic fields were parallel to each other and to the sample face, orthogonal to the hexagonal c axis, see Fig. 1(a). Uniaxial tension p was produced by a calibrated spring.

We also performed a neutron scattering study of the dependence of the helical wavevector q of the HAFM phase on the tension applied in the absence of an external magnetic field. These measurements were carried out on the DN-2 time-of-flight diffractometer of the IBR-2 pulse reactor [37] (Dubna, JINR) in $2\theta = 90^\circ$ geometry employing a two-dimensional position-sensitive detector, and the same experimental cell in the close-cycle refrigerator. The hexagonal c axis of the sample was about 1.5° inclined to the sample face. Therefore it was possible to observe the (002) reflection and nearby magnetic satellites with the neutron beam illuminating the

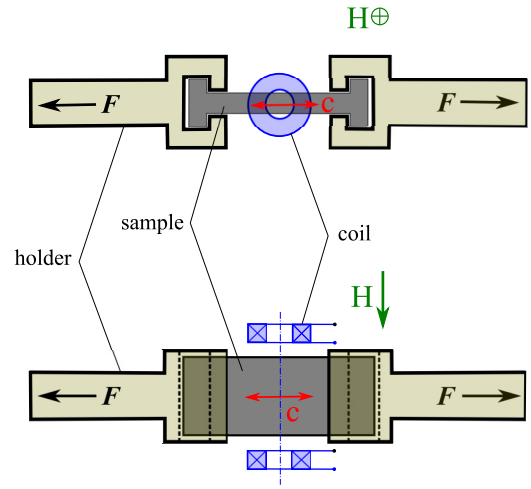

FIG. 1. Sketch of the experimental cell, side and top views. The probe ac magnetic field, parallel to the permanent magnetic field H, is orthogonal to the hexagonal c axis and parallel to the sample face.

sample face under this small angle, see sketch in Fig. 2 (angle exaggerated).

Owing to this unfavorable geometry, the effective sample surface was as low as ≈0.1 mm^2, and exposures about 10 hours were required to obtain the diffraction patterns. Patterns for the tensions $p = 0$ (without the loading cell), 160 bar (8 hours exposure), and 310 bar (12 hours exposure) were obtained at temperatures 2.2 K below the respective T_N, i.e., at $T = 0.99T_N$ (see Sec. II B). These patterns are presented in Fig. 3 with 0.8 of the central (nuclear) peaks subtracted to highlight the magnetic satellites. Lines correspond to the fits "Gaussian central peak and two equal symmetrical Gaussian satellites." The width of these satellites increases rapidly with an increase of tension p, so no reliable patterns were obtained at higher values of p. The decline in satellite q values with tension increase is nevertheless evident.

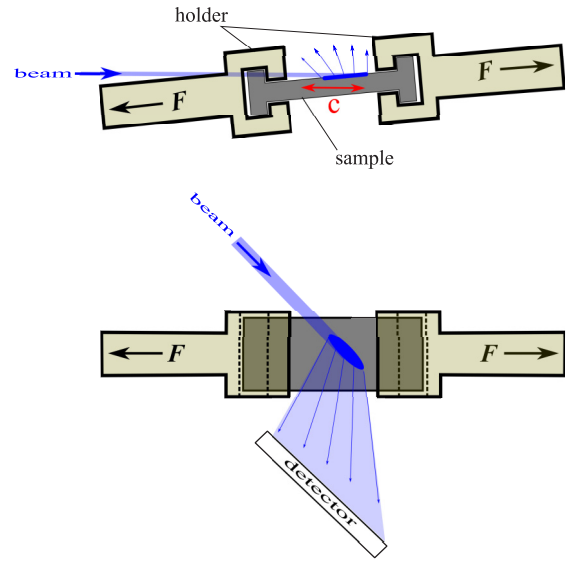

FIG. 2. Sketch of the neutron diffraction geometry, side (inclination exaggerated) and top views.

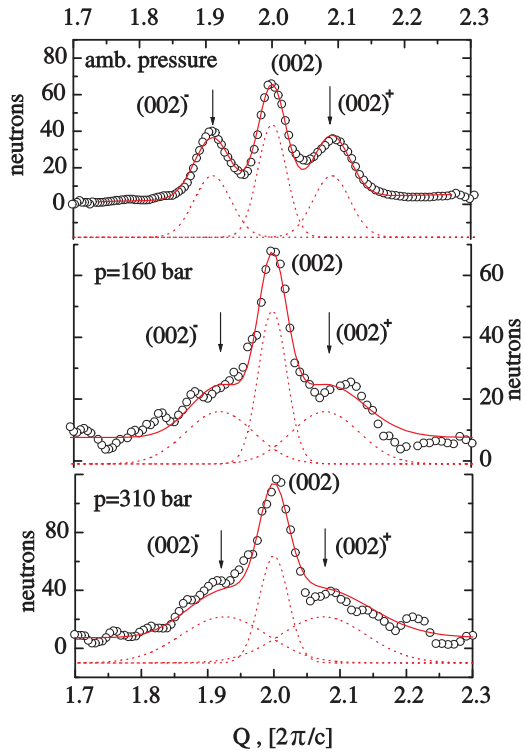

FIG. 3. Resulting diffraction patterns, each obtained 2.2 K below the respective Néel temperature, for the three tension values. 0.8 of the (002) central peak subtracted to highlight the $(002)^+$ and $(002)^-$ magnetic satellites (marked by arrows). Fitted by "Gaussian central peak and two symmetrical Gaussian satellites" functions (dashed and solid lines).

B. Magnetic susceptibility

The temperature dependence of $\chi_{ac}(T)$ in zero magnetic field, obtained on cooling, is presented in Fig. 4(a) for zero tension $p = 0$ (Tb orders magnetically into HAFM phase at $T_N = 231.2$ K and turns into the FM phase at $T_1 = 226.5$ K) and for $p = 720$ bar, the highest tension applied (Tb orders directly into the FM phase at $T_C = 232.3$ K). The characteristic anomaly associated with the occurrence of the HAFM phase at zero tension is clear, as is its absence at $p = 720$ bar where the HAFM phase is completely suppressed by applied tension, see Ref. [36] for the details.

The anomaly associated with the HAFM phase, the main interest of our study, is as weak as 5% of the total χ_{ac} value near T_N. It is less than the χ_{ac} hysteresis with both the magnetic field and temperature (up to 15%), which could mask the studied transitions. To avoid such hysteresis effects, all the $\chi_{ac}(T)$ dependencies were obtained on cooling from the paramagnetic state with the same rate 0.7 K/min. For the same reason, all the $\chi_{ac}(H)$ dependencies were obtained on the field increase after zero field cooling. All these dependencies are completely reversible with respect to the tension applied.

$\chi_{ac}(T)$ data in the various magnetic field H values are presented in Fig. 4(b) both for ambient pressure $p = 0$ and for the applied uniaxial tension $p = 720$ bar. Each pair of $\chi_{ac}(T)$ dependencies was obtained at the same H value, labeled on the curves, and plotted against reduced temperature T/T_{ord}. This comparison highlights the anomaly associated with the

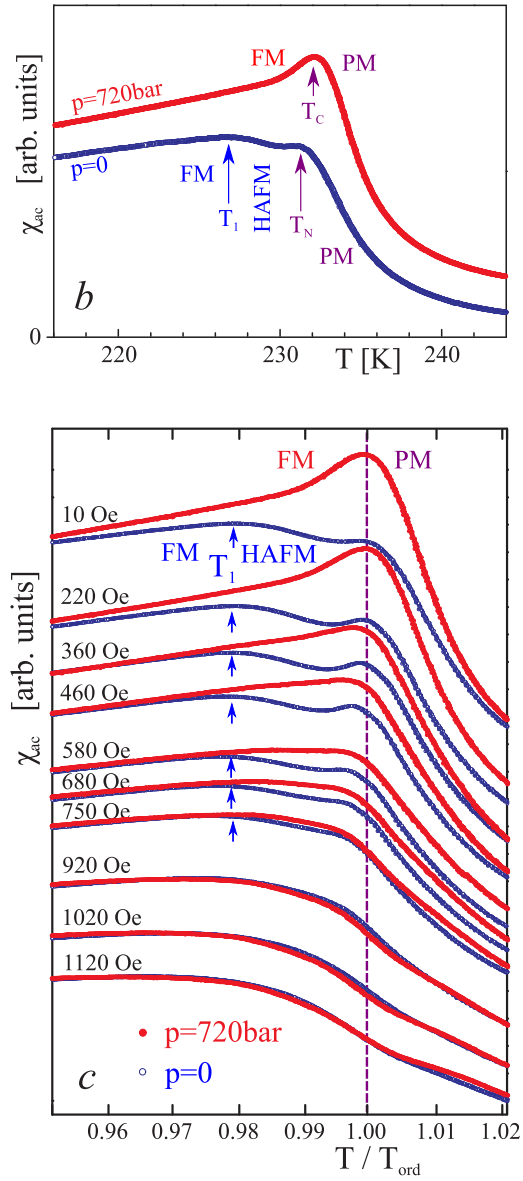

FIG. 4. (a) Temperature dependence of the magnetic susceptibility $\chi_{ac}(T)$ for the Tb single crystal in zero magnetic field under ambient pressure $p = 0$ (open dots) and under uniaxial tension $p = 720$ bar (solid dots). $T_C = 232.3$ K is the Curie temperature, $T_N = 231.2$ K is the Néel temperature, and $T_1 = 226.5 \pm 0.5$ K is the temperature of the "helical antiferromagnet-ferromagnet" transition. (b) Dependencies of the magnetic susceptibility χ_{ac} on the reduced temperature T/T_{ord}, obtained under zero tension (open dots, magnetic ordering into the helical phase) and under tension $p =$ 720 bar (solid dots, magnetic ordering into the ferromagnetic phase). Each pair of the dependencies are obtained in the same permanent magnetic field H, labeled over the curves. The curves are shifted vertically by an amount proportional to the applied field H for the sake of clarity. All dependencies were obtained on cooling from the paramagnetic phase with the same rate. Arrows mark T_1, the temperature of the "helical antiferromagnet-ferromagnet" transition. Abbreviations: PM-paramagnetic, HAFM-helical antiferromagnetic, and FM-ferromagnetic phases.

HAFM phase and its suppression caused by increasing the magnitude of the applied magnetic field. Unexpectedly, T_1

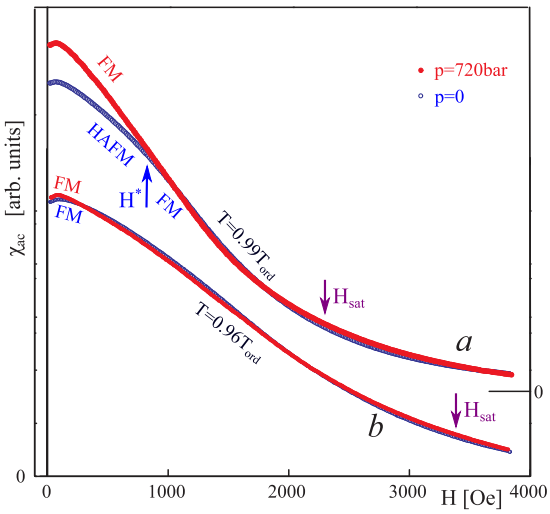

FIG. 5. Typical magnetic field dependencies of the magnetic susceptibility $\chi_{ac}(H)$, obtained at zero tension (open dots, magnetic ordering into a helical antiferromagnetic phase) and under tension $p = 720$ bar (solid dots, magnetic ordering into a ferromagnetic phase). At temperatures (a) $T = 0.99T_{ord}$ (229.3 and 230.5 K, respectively, shifted vertically for clarity) the initial magnetic states are HAFM and FM respectively, and at (b) $T = 0.96T_{ord}$ (222.2 and 221.9 K respectively) the sample is always ferromagnetic. All measurements were taken in increasing magnetic field after zero field cooling. Arrows mark the transition from the helical to the ferromagnetic phase for $p = 0$ at H^* and saturation at H_{sat} (approximate values). Abbreviations: HAFM-helical antiferromagnetic and FM-ferromagnetic phases.

appeared to be almost field independent. For H field values above 800 Oe the dependencies for $p = 0$ and 720 bar coincide within experimental accuracy, while at the lower H values the anomaly associated with the transition at T_1 for $p = 0$ is clear. An inspection of the figure allowed us to associate a threshold value of $H^* \approx 800 \pm 100$ Oe.

In Fig. 5, the typical dependence of the susceptibility, $\chi_{ac}(H)$, on increasing magnetic field after zero field cooling, is presented for zero uniaxial tension $p = 0$ and for $p = 720$ bar. The figure, therefore, highlights the anomaly associated with the HAFM phase in comparison with the ferromagnetically ordered one. The pair of curves (a) (both shifted up for clarity), obtained at $T = 0.99T_{ord}$, clearly differ at $H < H^* \approx 800$ Oe and coincide above this field value. In contrast, the pair of curves (b), obtained at $T = 0.96T_{ord}$ well below T_1, correspond to the FM phase and coincide within experimental accuracy over the whole magnetic field range. Therefore we conclude that the observed difference in case (a), subtle but clear, corresponds to the presence of the HAFM phase for $p = 0$, while this phase is absent for $p = 720$ bar. The $H^* = 800$ Oe critical value agrees well with that obtained from the $\chi_{ac}(T)$ data in Fig. 4. We highlight the absence of additional anomalies associated with any presumed intermediate fan state.

C. Temperature-magnetic field phase diagrams and demagnetizing field

The resulting experimental H-T magnetic phase diagrams are presented in Fig. 6(a) for $p = 720$ bar and in Fig. 6(b) for zero tension $p = 0$. The region associated with the HAFM phase is unexpectedly rectangular in shape and consequently it may be characterized by a single value of H^*. This shape persists within the entire tension range of $p < p^*$, where p^* is the critical value of the tension at which the HAFM state is fully suppressed.

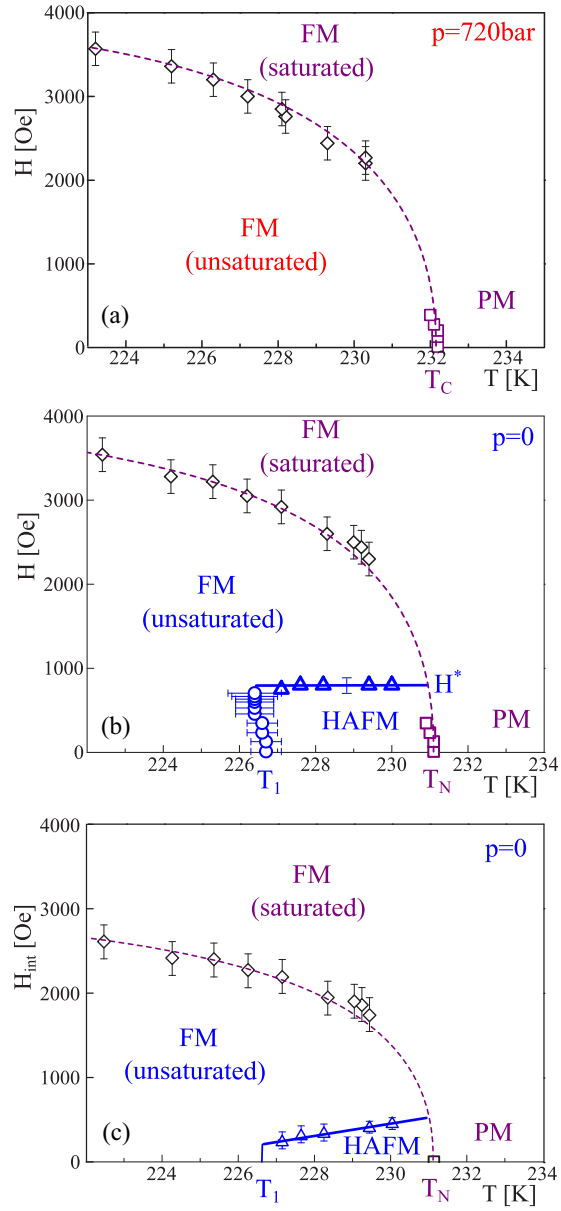

FIG. 6. Temperature-magnetic field phase diagrams for Tb with the magnetic field H orthogonal to the hexagonal axis: (a) for tension $p = 720$ bar, (b) for zero tension $p = 0$, (c) for zero tension $p = 0$ after correction for demagnetization. Squares: T_{ord} (either Néel or Curie temperature), circles: T_1, horizontal line: H^*; obtained from $\chi_{ac}(T)$ data. Triangles: H^*, diamonds: H_{sat}; obtained from $\chi_{ac}(H)$ data. Abbreviations: PM-paramagnetic, HAFM-helical antiferromagnetic, and FM-ferromagnetic (saturated and unsaturated) phases. Lines are guides for the eye.

The values of the demagnetizing magnetic field, even in this favorable geometry, are comparable to H^*, so a correction for demagnetization is necessary. The uniform magnetization

M in this geometry produces a demagnetizing field $-D \times 4\pi M$ with demagnetizing factor $D = 0.07$ in the center of the sample, while ellipsoid of the same proportions as our sample provides $D = 0.10$. Figure 6(c) presents the magnetic phase diagram shown in Fig. 6(b) for the zero tension $p = 0$, corrected for demagnetization employing $D = 0.10$ value and magnetization data from [24]. The values of H^* that we have obtained behave similarly to other experimental studies [20–24] but are slightly higher. It would require the unrealistically high demagnetizing factor $D \approx 0.2$ to reach a better agreement.

Figure 6 also shows the value of the magnetic field at which the magnetization saturates, H_{sat}. The dependence of H_{sat} on temperature for $p = 0$ exhibits no anomalies near T_1 and coincides with its peer for $p = 720$ bar within experimental accuracy, as well as for all the other values of the tension studied. An additional set of $\chi_{ac}(T)$ dependencies over the whole tension range was obtained at $H = 1100$ Oe, just above the highest value of H^*. All these dependencies, both below and above p^*, coincide within the experimental accuracy up to a regular shift in temperature with the rate 1.0 K/kbar. There is no sign of additional anomalies associated with the stabilization of an intermediate phase. We thus identify the magnetic phase between H^* and H_{sat} as an unsaturated FM state and conclude that a fan phase does not stabilize.

D. Magnetic phase diagrams for the pressure and role of the Fermi surface topology

Figure 7 summarizes the dependence on uniaxial tension p of our experimental results. Panel (a) presents the T-p magnetic phase diagram of Tb at zero magnetic field. T_{ord} and T_1 are obtained from $\chi_{ac}(T)$ dependencies shown in Fig. 4(b) for different values of the tension. The HAFM phase is clearly suppressed by a critical value with an approximate magnitude of $p^* = 580$ bar. For tensions larger than p^* we observe the complete elimination of the HAFM phase, in agreement with Ref. [36]. Interestingly, we have obtained a linear behavior for the ordering temperature (T_{ord}) at which the paramagnetic state becomes unstable to the formation of both the ferromagnetic and the HAFM states, i.e., at T_c and T_N, respectively. On the other hand, the HAFM-ferromagnetic transition temperature (T_1) shows a deviation from linearity with tension p.

The $\chi_{ac}(T)$ and $\chi_{ac}(H)$ curves have been used to obtain the critical magnetic field $H^*(p)$, shown in Fig. 7(b). $H^*(p)$ decreases from roughly 800 Oe at $p = 0$ and becomes zero at p^*. The solid line in this panel is a guide for the eye. The neutron diffraction measurements presented in section II A have been used to obtain the tension dependence of the reduced helical wave vector $q(p)$ right below the magnetic ordering temperature, which we show in Fig. 7(c). For increasing values of tension the wave vector decreases, i.e., p causes an increase of the period in real space of the HAFM state until the FM state is eventually stabilized above p^*. The dashed line in Fig. 7(c) follows a characteristic behavior of the nesting vector against pressure, which links to $q(p)$, in the vicinity of a Lifshitz transition. This corresponds to a qualitative change of the FS geometry and a continuous change of this wavevector from a finite to a vanishing value at p^*. p^* is, therefore, the

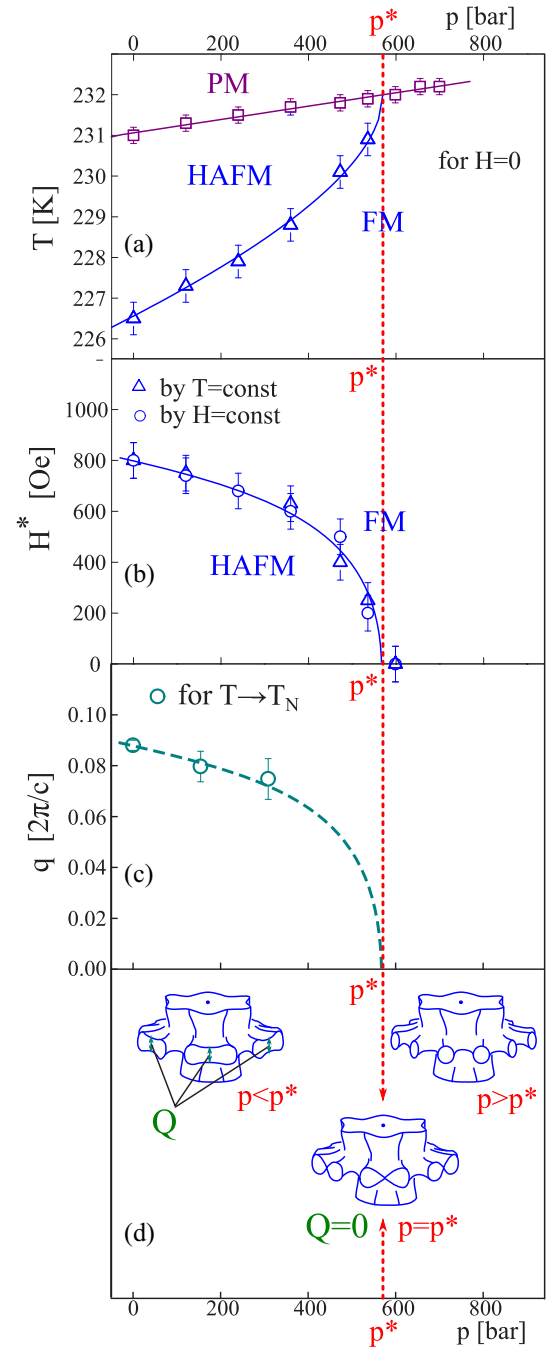

FIG. 7. (a) Uniaxial tension-temperature magnetic phase diagram for Tb in zero magnetic field. Squares: magnetic ordering temperature T_{ord}, triangles: T_1. Curve is a guide for the eye. p^* is a critical value. (b) Uniaxial tension dependence of the critical magnetic field H^* (a single value is assumed for the each tension applied). Triangles: obtained from $\chi_{ac}(H)$, circles: from $\chi_{ac}(T)$ dependencies. Curve is a guide for the eye. (c) Uniaxial tension dependence of the helical wave vector q at $0.99T_N$. The dashed curve follows an expected behavior of the nesting vector Q of the Fermi surface undergoing a Lifshitz transition at p^*. (d) Sketches of the expected Fermi surface behavior in the vicinity of the Lifshitz transition at p^* in the paramagnetic state (double zone presentation). Q is a nesting vector, assumed equal to the magnetic helical wave vector q. Abbreviations: PM-paramagnetic, HAFM-helical antiferromagnetic, and FM-ferromagnetic phases.

value of the tension at which the Lifshitz transition occurs. Figure 7(d) represents a schematic of the corresponding evolution of the FS in the paramagnetic state of Tb under tension increase around this transition [32,35,36]. Here Q is a nesting vector that is roughly equal to the magnetic wave vector q and the origin for the helical magnetic ordering. The observed behavior of the transition temperature T_1, critical field H^*, and magnetic wave vector q in Tb under uniaxial tension follow the rootlike dependence characteristic of a Lifshitz transition.

III. THEORETICAL APPROACH

We now compare our results with an analysis from the density functional theory (DFT)-based disordered local moment (DLM) theory of finite temperature dependent magnetism [38–40]. Within this framework we model thermal fluctuations of the orientations of the local magnetic moments, referred to $\{\hat{\mathbf{e}}_n\}$ at sites n, fully from first-principles by picturing them as slowly evolving classical parameters that robustly emerge from the underlying and faster many-electron interactions [38]. In Tb they are predominantly set up by the occupied f-electron states. The interactions among the highly localized $4f$ electrons are treated by implementing the local self-interaction correction (LSIC) [41,42]. Statistical averages over different disordered magnetic configurations $\{\hat{\mathbf{e}}_n\}$ provide the magnetic Gibbs free energy of materials [40],

$$\mathcal{G} = E(\{\mathbf{m}_n\}, \mathbf{H}, p) - TS_{\text{mag}}(\{\mathbf{m}_n\}), \tag{1}$$

where E is an internal magnetic energy that is available from magnetically constrained DFT calculations and contains the effect of an applied external magnetic field $\mathbf{H}$ and an applied mechanical stress p. S_{mag} is the entropy associated with the disorder of the local moment orientations $\{\hat{\mathbf{e}}_n\}$. $\mathcal{G}$ naturally depends on magnetic order parameters

$$\{\mathbf{m}_n \equiv \langle \hat{\mathbf{e}}_n \rangle\}, \tag{2}$$

which follows from the statistical averages over $\{\hat{\mathbf{e}}_n\}$, denoted by $\langle \dots \rangle$, that are required to obtain the thermal properties.

We have shown that using Gd as a magnetic prototype for other heavy rare earth elements (HREs) with contracted lattice parameters consistent with the lanthanide contraction and applying the DFT-DLM theory results in a very good description of their magnetism [8,30] as well as that of their alloys and compounds [43–46]. This is due largely to the common valence electronic structure [8,30]. In this work, we build on this treatment and use again Gd as the magnetic prototype of Tb. One advantage of this strategy is that crystal field and spin-orbit effects are very small for Gd and so can be neglected.

In this theoretical model, we have found that Tb passes from the PM to a HAFM phase at T_N and then undergoes a first order transition to a FM phase at T_1 just below T_N [8,30]. We extend this study here. In the absence of an external magnetic field, the HAFM phase is not distorted. For this situation, we calculate the temperature dependence and stability of the HAFM and ferromagnetic states, and the effect of an applied tension p, by introducing two order parameters, m_{HAFM} and m_{FM}. These describe arrangements of the local order parameters $\{\mathbf{m}_n\}$ characterising helical antiferromagnetic and ferromagnetic order respectively. Since the $\{\hat{\mathbf{e}}_n\}$ are unit vectors, from Eq. (2) one can see that $m_{\text{HAFM}} = 1$ ($m_{\text{FM}} = 1$) occurs when $\{\hat{\mathbf{e}}_n\}$ do not thermally fluctuate, i.e., the system is at the absolute zero temperature and a fully ordered HAFM (FM) state is stable. Decreasing values of m_{HAFM} or m_{FM} describe larger and more frequent thermal fluctuations of the local moment orientations. The fully disordered, paramagnetic, limit thus corresponds to $m_{\text{HAFM}} = m_{\text{FM}} = 0$.

Our DFT-DLM theory [38,39] for the HREs provides the internal magnetic energy in the following form [8] for both the HAFM and FM states:

$$\begin{aligned} E_{\text{FM}} &= -\mathcal{S}^{(2)}_{\text{FM}} m^2_{\text{FM}} - \mathcal{S}^{(4)}_{\text{FM}} m^4_{\text{FM}}, \\ E_{\text{HAFM}} &= -\mathcal{S}^{(2)}_{\text{HAFM}} m^2_{\text{HAFM}} - \mathcal{S}^{(4)}_{\text{HAFM}} m^4_{\text{HAFM}}, \end{aligned} \tag{3}$$

and the corresponding Gibbs free energies are then given by applying Eq. (1),

$$\begin{aligned} \mathcal{G}_{\text{FM}} &= E_{\text{FM}}(m_{\text{FM}}) - TS_{\text{mag}}(m_{\text{FM}}), \\ \mathcal{G}_{\text{HAFM}} &= E_{\text{HAFM}}(m_{\text{HAFM}}) - TS_{\text{mag}}(m_{\text{HAFM}}). \end{aligned} \tag{4}$$

$\{\mathcal{S}^{(2)}_{\text{FM}}, \mathcal{S}^{(4)}_{\text{FM}}, \mathcal{S}^{(2)}_{\text{HAFM}}, \mathcal{S}^{(4)}_{\text{HAFM}}\}$ are material-dependent free energy coefficients [40]. We point out that analytical expressions for the entropy terms in Eq. (4) are directly provided by a mean-field treatment in our theory [40]. We calculate $\{\mathcal{S}^{(2)}_{\text{FM}}, \mathcal{S}^{(4)}_{\text{FM}}, \mathcal{S}^{(2)}_{\text{HAFM}}, \mathcal{S}^{(4)}_{\text{HAFM}}\}$ for different lattice parameters that directly follow the effect of uniaxial tension that we have measured experimentally, i.e., for different crystal structures corresponding to different uniaxial tensions. Once all the coefficients and parts of Eq. (4) have been obtained, each of these equations is minimized with respect to m_{FM} and m_{HAFM} at different temperatures and lattice parameters. The magnetic state with the lower free energy is considered as the more stable one. Further details of our Gibbs free energy calculations from the DFT-DLM framework are given in Refs. [8,40].

The calculations for $p = 0$ use hcp lattice parameters that result in a temperature span of $T_N - T_1 \approx 5$ K, to align with the experimental measurements. We then model the effect of increasing values of p by applying an uniaxial strain to these lattice parameters such that there is a match with the exact experimental lattice distortion. In particular, $a = b$ decreases by 0.03% and c increases by 0.07% after applying $p = 700$ bar. The free energy coefficients that we have computed for our model of Tb following this prescription and characterizing the internal magnetic energy in Eq. (3) are

$$\begin{aligned} \mathcal{S}^{(2)}_{\text{FM}} &= 35.26\ [\text{meV}] + 0.20\left[\frac{\text{meV}}{\text{kbar}}\right] \times p, \\ \mathcal{S}^{(2)}_{\text{HAFM}} &= 35.36\ [\text{meV}] + 4 \times 10^{-3}\left[\frac{\text{meV}}{\text{kbar}}\right] \times p, \end{aligned} \tag{5}$$

and

$$\begin{aligned} \mathcal{S}^{(4)}_{\text{FM}} &= 2.0\ [\text{meV}] + 5 \times 10^{-4}\left[\frac{\text{meV}}{\text{kbar}}\right] \times p, \\ \mathcal{S}^{(4)}_{\text{HAFM}} &= -1.4\ [\text{meV}] + 2 \times 10^{-3}\left[\frac{\text{meV}}{\text{kbar}}\right] \times p. \end{aligned} \tag{6}$$

Equation (5) confirms how close the two magnetic phases are in energy and that these leading quadratic terms have a positive dependence on p, in agreement with our experimental diagram in Fig. 7(a). We point out that $\mathcal{S}^{(2)}_{\text{FM}}$ shows a much larger dependence on p. On the other hand, the

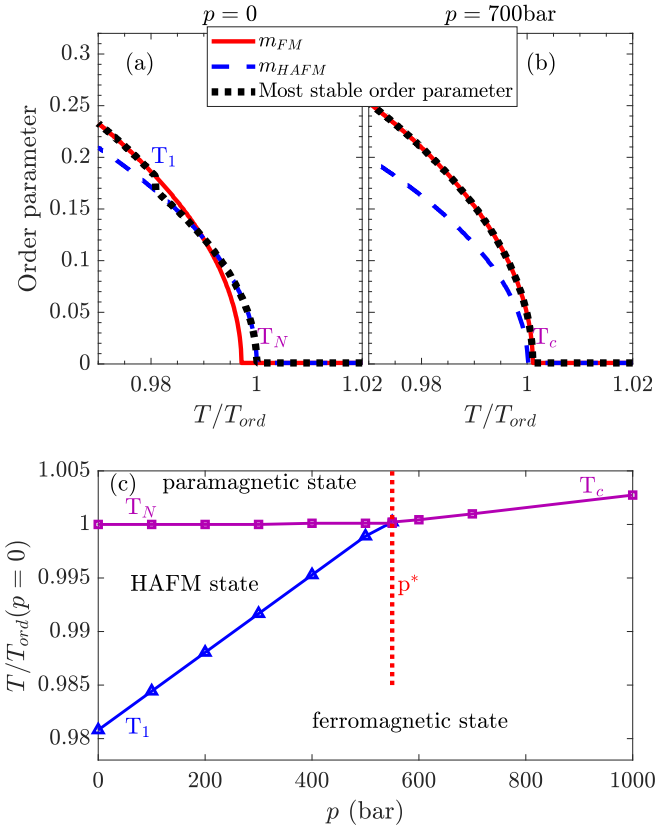

FIG. 8. *Ab initio* calculation of the temperature and tension dependence of the magnetic order parameters and transition temperatures between paramagnetic, ferromagnetic, and HAFM phases of Tb obtained by computing and minimizing the Gibbs free energy. [(a) and (b)] m_{FM} and m_{HAFM}, the magnetic order parameters for the ferromagnetic and HAFM phases, as functions of temperature. The dotted black line indicates the more stable magnetic phase. (c) Tension-temperature magnetic phase diagram. The vertical dotted red line indicates the predicted critical value of the tension p^* at which the HAFM is fully suppressed. Axis for the temperature are given normalized to T_{ord} at $p = 0$, i.e., T_N.

quartic coefficients in Eq. (6) are very small for both the ferromagnetic and HAFM states, which is in sharp contrast with heavier rare earth elements, such as Dy and Ho [8]. However, their presence is still the fundamental origin of the HAFM-ferromagnetic phase transition at T_1.

Figures 8(a) and 8(b) show the corresponding magnetic order parameters associated with the ferromagnetic and HAFM states, m_{FM} (continuous red line) and m_{HAFM} (dashed blue line), respectively. We obtain them by minimizing the individual Gibbs free energies given in Eq. (4) at different temperatures normalized to T_{ord} at $p = 0$, i.e., T_N. The dotted black line is used to indicate the magnetic phase with the lower free energy, which corresponds to the more stable one. In good agreement with the experimental measurements, our calculations demonstrate that the change of the crystal structure induced by $p \approx 600$ bar is sufficient to cause a suppression of the HAFM state. Furthermore monitoring how T_1 and T_{ord} (either T_c or T_N) vary provides a first-principles estimation of the corresponding magnetic phase diagram, which we show in Fig. 8(c). It agrees very well with the experimental

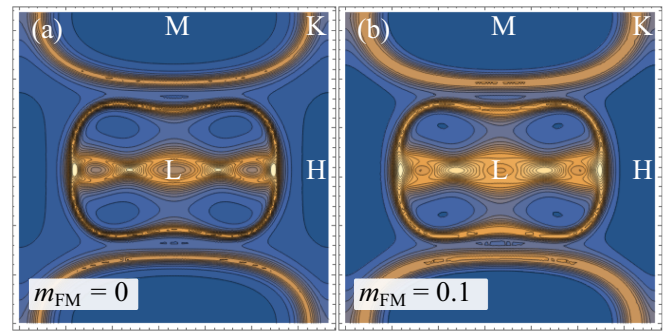

FIG. 9. The Bloch spectral function for the $HKLM$ plane at the Fermi energy calculated in (a) the paramagnetic state and (b) the FM state (for $m_{\mathrm{FM}} = 0.1$), of Tb using Gd as its magnetic prototype when $p = 0$. The second figure indicates the effect of strong short-range FM correlations on the FS reducing the nesting.

one shown in Fig. 7(a). We correctly find that the change of the HAFM-FM transition temperature with p is positive, giving a value of $dT_1/dp = 10$ K/kbar ($dT_1/dp \approx 7.5$ K/kbar for low tensions in experiment). However, we compute an almost constant Néel temperature while experimentally an increase is evident.

A discrepancy between the *ab initio* theory model and the experimental measurements arises, however, from the pressure dependence of the wave vector which describes the helical magnetic order of the HAFM phase. In the theory as in the experiment, the wave vector is set by nesting in the paramagnetic ($m_{\mathrm{FM}} = m_{\mathrm{HAFM}} = 0$) Fermi surface of the valence electrons. In our calculations, this value is approximately equal to $q \approx 0.19\,\frac{2\pi}{c}$ as shown in Fig. 9(a), although nesting is already fairly weak for the case of Tb. However, we have found that q shows negligible decrease for the values of p that suppress the HAFM phase. Indeed our calculations find a Lifshitz FS transition to occur at a higher tension [30,32]. The theory shows instead a discontinuous change of q at p^* where the free energy for the FM phase drops below that of the HAFM state. Increasing p weakens the incommensurate HAFM magnetic correlations relative to the FM ones but does not remove them entirely at p^*. In Ref. [8], we showed how magnetic field application or growing long-range ferromagnetic order destroys the FS nesting in the HREs and triggers the first order transition from HAFM to FM via a fan phase. In the case of Tb, where the region between the phases is so narrow and the separation between T_1 and T_N rather small, it is likely that the Lifshitz FS transition not being coincidental with the HAFM-FM transition with applied tension is a shortcoming of our mean field treatment of the magnetic correlations. Close to T_{ord} both FM and HAFM correlations are strong and the former large enough in extent to affect the valence electronic structure and weaken the FS nesting. Figure 9(b) illustrates this point by showing how the FS changes when an overall small FM magnetic order $m_{FM} = 0.1$ is present.

IV. CONCLUSION

The temperature-magnetic field phase diagram and wave vector characterizing the helical incommensurate

antiferromagnetic state of a terbium single crystal have been studied as functions of applied uniaxial tension along the hexagonal c axis, with a magnetic field applied within the basal plane. The region associated with the helical antiferromagnetic phase has been tracked to its collapse under tension $p^* \approx 600$ bar. No evidence of an intermediate "fan phase" has been observed. The dependencies of the characteristic temperature, critical magnetic field and helical wave vector on tension are consistent with the occurrence of a strain-induced Lifshitz transition at p^*, being responsible for this collapse. A finite-temperature *ab initio* theory using a Gd prototypical model of the heavy rare earth metals adapted for Tb has been applied to analyze the results. The theory provides a temperature-tension magnetic phase diagram which agrees very well with our experimental measurements. It does not, however, find a Lifshitz transition in the FS at the critical tension p^* although nesting of Tb's FS is weak but evident. This discrepancy highlights how it is important to account for the effects of both short- and long-range ferromagnetic order on the valence electrons in Tb close to T_{ord}.

ACKNOWLEDGMENTS

A.Vl.A. is grateful to O. D. Chistiakov for the provision of the sample. J.B.S. acknowledges support from the PRETA-MAG project, funded by the UK Engineering and Physical Sciences Research Council, Grant No. EP/M028941/1.

[1] J. Jensen and A. R. Mackintosh, *Rare Earth Magnetism: Structures and Excitations* (Clarendon Oxford, 1991).

[2] W. C. Koehler, H. R. Child, E. O. Wollan, and J. W. Cable, Some magnetic structure properties of terbium and of terbiumyttrium alloys, J. Appl. Phys. **34**, 1335 (1963).

[3] M. K. Wilkinson, W. C. Koehler, E. O. Wollan, and J. W. Cable, Neutron diffraction investigation of magnetic ordering in dysprosium, J. Appl. Phys. **32**, S48 (1961).

[4] W. C. Koehler, J. W. Cable, M. K. Wilkinson, and E. O. Wollan, Magnetic structures of holmium. i. the virgin state, Phys. Rev. **151**, 414 (1966).

[5] W. C. Koehler, J. W. Cable, H. R. Child, M. K. Wilkinson, and E. O. Wollan, Magnetic structures of holmium. ii. the magnetization process, Phys. Rev. **158**, 450 (1967).

[6] D. R. Behrendt, S. Legvold, and F. H. Spedding, Magnetic properties of dysprosium single crystals, Phys. Rev. **109**, 1544 (1958).

[7] U Enz, Spin configuration and magnetization process in dysprosium, Physica **26**, 698 (1960).

[8] E. Mendive-Tapia and J. B. Staunton, Theory of Magnetic Ordering in the Heavy Rare Earths: *Ab Initio* Electronic Origin of Pair- and Four-Spin Interactions, Phys. Rev. Lett. **118**, 197202 (2017).

[9] R. Herz and H. Kronmüller, Field-induced magnetic phase transitions in dysprosium, J. Magn. Magn. Mater. **9**, 273 (1978).

[10] V. I. Zverev, A. M. Tishin, Z. Min, Y. Mudryk, K. A. G. Jr, and V. K. Pecharsky, Magnetic and magnetothermal properties, and the magnetic phase diagram of single-crystal holmium along the easy magnetization direction, J. Phys.: Condens. Matter **27**, 146002 (2015).

[11] R. A. Cowley, R. C. C. Ward, M. R. Wells, M. Matsuda, and B. Sternlieb, The magnetic structure and phase transitions of holmium-yttrium alloys, J. Phys.: Condens. Matter **6**, 2985 (1994).

[12] J. Yu, P. R. LeClair, G. J. Mankey, J. L. Robertson, M. L. Crow, and W. Tian, Exploring the magnetic phase diagram of dysprosium with neutron diffraction, Phys. Rev. B **91**, 014404 (2015).

[13] M. Akhavan and H. A. Blackstead, Magnetoresistance and field-induced phase transitions in the helical and conical states of holmium, Phys. Rev. B **13**, 1209 (1976).

[14] M. C. Lee and M. Levy, Longitudinal ultrasonic attenuation in the spin spiral state of single crystal holmium, J. Phys. Chem. Solids **34**, 995 (1973).

[15] C. Isci and S. B. Palmer, An ultrasonic study of the magnetic phases of dysprosium, J. Phys. F **8**, 247 (1978).

[16] A. V. Andrianov, V. D. Buchel'nikov, A. N. Vasil'ev, Yu. P. Gaidukov, and V. G. Shavrov, Electromagnetic excitation of ultrasound in a dysprosium single crystal, Zh. Eksp. Teor. Fiz. **97**, 1674 (1990) [Sov. Phys. JETP **70**, 944 (1990)].

[17] H. Ohsumi, K. Tajima, N. Wakabayashi, Y. Shinoda, K. Kamishima, and T. Goto, Crystal lattice changes induced by magnetic field and helifan structure in holmium metal, J. Phys. Soc. Jpn. **66**, 1896 (1997).

[18] Y. Kida, K. Tajima, Y. Shinoda, K. Hayashi, and H. Ohsumi, Effect of magnetic field on crystal lattice in dysprosium studied by x-ray diffraction, J. Phys. Soc. Jpn. **68**, 650 (1999).

[19] A. S. Chernyshov, A. O. Tsokol, A. M. Tishin, K. A. Gschneidner, and V. K. Pecharsky, Magnetic and magnetocaloric properties and the magnetic phase diagram of single-crystal dysprosium, Phys. Rev. B **71**, 184410 (2005).

[20] R. D. Greenough and N. F. Hettiarachchi, Critical fields and commensurate turn angle effects in terbium, J. Magn. Magn. Mater. **31-34**, 178 (1983).

[21] A. Drillat, J. Baruchel, S. Bates, and S. B. Palmer, Negative evidence for incommensurate-commensurate effects in the temperature dependence of the helical turn angle and the critical field of Tb, Dy and Ho, J. Magn. Magn. Mater. **44**, 232 (1984).

[22] D. C. Jiles, S. B. Palmer, D. W. Jones, S. P. Farrant, and K. A. Gschneidner, Magnetoelastic properties of high-purity single-crystal terbium, J. Phys. F **14**, 3061 (1984).

[23] S. A. Nikitin, A. M. Tishin, R. V. Bezdushnyi, Yu. I. Spichkin, and S. V. Red'ko, Effect of uniform pressure on magnetization and magnetic phase diagram of terbium single crystal, J. Magn. Magn. Mater. **92**, 397 (1991).

[24] V. I. Zverev, A. M. Tishin, A. S. Chernyshov, Y. Mudryk, K. A. G. Jr, and V. K. Pecharsky, Magnetic and magnetothermal properties and the magnetic phase diagram of high purity single crystalline terbium along the easy magnetization direction, J. Phys.: Condens. Matter **26**, 066001 (2014).

[25] W. M. Lomer, Electronic structure of chromium group metals, Proc. Phys. Soc. **80**, 489 (1962).

[26] I. E. Dzyaloshinski, The theory of helicoidal structures in antiferromagnets. ii. metals, Sov. Phys. JETP **20**, 223 (1965).

[27] S. B. Dugdale, H. M. Fretwell, M. A. Alam, G. Kontrym-Sznajd, R. N. West, and S. Badrzadeh, Direct Observation and Calipering of the "Webbing" Fermi Surface of Yttrium, Phys. Rev. Lett. **79**, 941 (1997).

[28] V. Thakor, J. B. Staunton, J. Poulter, S. Ostanin, B. Ginatempo, and E. Bruno, First-principles relativistic theory of the magnetic response of paramagnetic metals: Application to yttrium and scandium, Phys. Rev. B **68**, 134412 (2003).

[29] L. Nordström and A. Mavromaras, Magnetic ordering of the heavy rare earths, Europhys. Lett. **49**, 775 (2000).

[30] I. D. Hughes, M. Däne, A. Ernst, W. Hergert, M. Lüders, J. Poulter, J. B. Staunton, A. Svane, Z. Szotek, and W. M. Temmerman, Lanthanide contraction and magnetism in the heavy rare earth elements, Nature (London) **446**, 650 (2007).

[31] S. J Crowe, S. B Dugdale, Z. Major, M. A Alam, J. A. Duffy, and S. B. Palmer, Electronic topological transitions, magnetic ordering and the fermi surfaces of y and the heavy rare earths, Europhys. Lett. **65**, 235 (2004).

[32] A. Vl. Andrianov, O. A. Savel'eva, E. Bauer, and J. B. Staunton, Squeezing the crystalline lattice of the heavy rare-earth metals to change their magnetic order: Experiment and ab initio theory, Phys. Rev. B **84**, 132401 (2011).

[33] K. M. Döbrich, A. Bostwick, J. L. McChesney, K. Rossnagel, E. Rotenberg, and G. Kaindl, Fermi-Surface Topology and Helical Antiferromagnetism in Heavy Lanthanide Metals, Phys. Rev. Lett. **104**, 246401 (2010).

[34] I. L. M. Locht, Y. O. Kvashnin, D. C. M. Rodrigues, M. Pereiro, A. Bergman, L. Bergqvist, A. I. Lichtenstein, M. I. Katsnelson, A. Delin, A. B. Klautau, B. Johansson, I. Di Marco, and O. Eriksson, Standard model of the rare earths analyzed from the hubbard i approximation, Phys. Rev. B **94**, 085137 (2016).

[35] I. M. Lifshits, Anomalies of electron characteristics of a metal in the high pressure region, Sov. Phys. JETP **11**, 1130 (1960).

[36] A. Vl. Andrianov, D. I. Kosarev, and A. I. Beskrovnyi, Helical magnetic ordering in tb completely suppressed by uniaxial tension: Evidence of electronic topological transition and support for the nesting hypothesis, Phys. Rev. B **62**, 13844 (2000).

[37] A. M. Balagurov, A. I. Beskrovnyy, V. V. Zhuravlev, G. M. Mironova, I. A. Bobrikov, D. Neov, and S. G. Sheverev, Neutron diffractometer for real-time studies of transient processes at the IBR-2 pulsed reactor, J. Surf. Invest. X-ray, Synchrotron Neutron Tech. **10**, 467 (2016).

[38] B. L. Gyorffy, A. J. Pindor, J. Staunton, G. M. Stocks, and H. Winter, A first-principles theory of ferromagnetic phase transitions in metals, J. Phys. F **15**, 1337 (1985).

[39] J. B. Staunton, R. Banerjee, M. dos Santos Dias, A. Deak, and L. Szunyogh, Fluctuating local moments, itinerant electrons, and the magnetocaloric effect: Compositional hypersensitivity of FeRh, Phys. Rev. B **89**, 054427 (2014).

[40] E. Mendive-Tapia and J. B. Staunton, Ab initio theory of the gibbs free energy and a hierarchy of local moment correlation functions in itinerant electron systems: The magnetism of the Mn_3 A materials class, Phys. Rev. B **99**, 144424 (2019).

[41] M. Lüders, A. Ernst, M. Däne, Z. Szotek, A. Svane, D. Ködderitzsch, W. Hergert, B. L. Györffy, and W. M. Temmerman, Self-interaction correction in multiple scattering theory, Phys. Rev. B **71**, 205109 (2005).

[42] C. E. Patrick and J. B. Staunton, Rare-earth/transition-metal magnets at finite temperature: Self-interaction-corrected relativistic density functional theory in the disordered local moment picture, Phys. Rev. B **97**, 224415 (2018).

[43] L. Petit, D. Paudyal, Y. Mudryk, K. A. Gschneidner, V. K. Pecharsky, M. Lüders, Z. Szotek, R. Banerjee, and J. B. Staunton, Complex Magnetism of Lanthanide Intermetallics and the Role of Their Valence Electrons: *Ab Initio* Theory and Experiment, Phys. Rev. Lett. **115**, 207201 (2015).

[44] C. E. Patrick, S. Kumar, G. Balakrishnan, R. S. Edwards, M. R. Lees, E. Mendive-Tapia, L. Petit, and J. B. Staunton, Rare-earth/transition-metal magnetic interactions in pristine and (Ni,Fe)-doped YCo_5 and $GdCo_5$, Phys. Rev. Materials **1**, 024411 (2017).

[45] C. E. Patrick, S. Kumar, G. Balakrishnan, R. S. Edwards, M. R. Lees, L. Petit, and J. B. Staunton, Calculating the Magnetic Anisotropy of Rare-Earth-Transition-Metal Ferrimagnets, Phys. Rev. Lett. **120**, 097202 (2018).

[46] E. Mendive-Tapia, D. Paudyal, L. Petit, and J. B. Staunton, First-order ferromagnetic transitions of lanthanide local moments in divalent compounds: An itinerant electron positive feedback mechanism and fermi surface topological change, Phys. Rev. B **101**, 174437 (2020).